Ejecta distribution patterns at Meteor Crater, Arizona: On the applicability of lithologic end-member deconvolution for spaceborne thermal infrared data of Earth and Mars

Michael S. Ramsey

Department of Geology and Planetary Science, University of Pittsburgh, Pittsburgh, Pennsylvania, USA

Received 26 November 2001; revised 20 January 2002; accepted 24 January 2002; published 27 August 2002

[1] A spectral deconvolution using a constrained least squares approach was applied to airborne thermal infrared multispectral scanner (TIMS) data of Meteor Crater, Arizona. The three principal sedimentary units sampled by the impact were chosen as end-members, and their spectra were derived from the emissivity images. To validate previous estimates of the erosion of the near-rim ejecta, the model was used to identify the areal extent of the reworked material. The outputs of the algorithm reveal subtle mixing patterns in the ejecta, identified larger ejecta blocks, and were used to further constrain the volume of Coconino Sandstone present in the vicinity of the crater. The availability of the multialtitude data set also provided a means to examine the effects of resolution degradation and quantify the subsequent errors on the model. These data served as a test case for the use of image-derived lithologic end-members at various scales, which is critical for examining thermal infrared data of planetary surfaces. The model results indicate that the Coconino Ss. reworked ejecta is detectable over 3 km from the crater. This was confirmed by field sampling within the primary ejecta field and wind streak. The areal distribution patterns of this unit imply past erosion and subsequent sediment transport that was low to moderate compared with early studies and therefore places further constraints on the ejecta degradation of Meteor Crater. It also provides an important example of the analysis that can be performed on thermal infrared data currently being returned from Earth orbit and expected from Mars in 2002. *INDEX TERMS:* 5420 Planetology: Solid Surface Planets: Impact phenomena (includes cratering); 5464 Planetology: Solid Surface Planets: Remote sensing; 5415 Planetology: Solid Surface Planets: Erosion and weathering; 5494 Planetology: Solid Surface Planets: Instruments and techniques; 6225 Planetology: Solar System Objects: Mars; *KEYWORDS:* Meteor Crater, thermal infrared, remote sensing, impact processes, Mars, erosion

1. Introduction

[2] Thermal infrared (TIR) remote sensing over the 8–12 μm region has been used as a tool to address a variety of geologic problems such as eolian sediment transport, volcanic landform interpretation, and detailed lithologic mapping [*Gillespie et al.*, 1984; *Abrams et al.*, 1991; *Hook et al.*, 1994; *Ramsey et al.*, 1999]. The ability to distinguish mineralogical differences is due to the fact that many materials display prominent absorption features within this wavelength region. In the context of geological studies, this feature corresponds to the vibrational frequencies of the SiO_4 and CO_4 anion group, making TIR remote sensing excellent for the study of silicate and carbonate rocks [*Lyon*, 1965; *Hunt*, 1980; *Salisbury and Walter*, 1989]. Further, unlike reflection in the visible/near-infrared portion of the spectrum, TIR spectra have been shown to be linearly additive, allowing the spectra to be interpreted as a linear mixture of its components or end-members [*Thomson and Salisbury*, 1993; *Ramsey*, 1996; *Ramsey and Christensen*, 1998; *Christensen et al.*, 2000a].

0148-0227/02/2001JE001827$09.00

[3] Mixing of radiant energy from surfaces occurs at all scales. Units larger than the fundamental image pixel size are easily traced spatially. Spectra from these pixels will have similar features that allow simple classification-based algorithms to identify the extent of these units. Examples of this multipixel or image-wide mixing on Earth include large tracts of vegetation, water bodies, and urban development; and on Mars, features such as large bedrock outcrops, sediment deposits and distinct albedo patterns are included. However, where individual components are smaller than the instrument resolution, subpixel mixing occurs. This intimate mixing takes place over much of an average TIR image and produces pixel-integrated spectra that vary in relation to the percentage of each end-member present. Areas of sparse vegetation where the plant size is smaller than the pixel and rock outcrops that are themselves mixtures of individual minerals, would both be typical examples. For cases such as these a subpixel deconvolution approach, based on a knowledge of the emission physics, is required.

[4] The use, viability, and potential of thermal infrared remote sensing for geological applications on Earth have been shown by many authors [*Kahle and Goetz*, 1983; *Gillespie et al.*, 1984; *Crowley and Hook*, 1996; *Ramsey et*

al., 1999]. Platforms with the capability of thermal infrared imaging became a reality in the 1960s with the TIROS meteorological satellites and continued with the short-lived NASA Heat Capacity Mapping Mission in 1978. For the next two decades, only the thematic mapper (TM) and the advanced very high resolution radiometer (AVHRR) instruments provided thermal infrared data from Earth orbit. These instruments acquire continuous data over much of the globe; however, data analysis is hindered by low spatial and spectral resolution. For example, TM had 120 m/pixel spatial resolution (60 m for the new enhanced TM instrument) with only one broadband channel between 10.5 μm and 12.5 μm, whereas the spatial resolution of AVHRR drops to 1.1 km/pixel, having only two channels spanning the 8–12 μm atmospheric window [*Sabins*, 1987].

[5] With the development of the NASA airborne thermal infrared multispectral scanner (TIMS) in 1981, high spatial resolution, multispectral TIR data became available [*Kahle and Goetz*, 1983]. Previously collected TIMS data still provide the only high spatial resolution TIR data for the study of geologic processes in many areas, despite being replaced by the more advanced airborne moderate-resolution imaging spectroradiometer/advanced spaceborne thermal emission and reflectance radiometer simulator (MASTER) in the late 1990s [*Hook et al.*, 2001]. The TIMS instrument has six spectral bands from 8–12 μm, producing a spatial resolution of 4–25 m/pixel as a function of the aircraft altitude [*Palluconi and Meeks*, 1985]. The TIMS also served as the first simulator for the ASTER instrument. ASTER, launched in December 1999 aboard the first Earth Observing Satellite (Terra), has 14 channels, 5 of which image in the thermal infrared region at 90 m/pixel resolution [*Kahle et al.*, 1991; *Yamaguchi et al.*, 1998; *Abrams*, 2000].

[6] In contrast to terrestrial remote sensing, high-resolution thermal infrared remote sensing of the Martian surface has been a reality from the earliest days of Mars exploration. The Mariner orbiters carried a hyperspectral TIR instrument, whereas the Viking orbiter's payload had the higher spatial resolution multispectral instrument [*Kieffer et al.*, 1977]. Both of these sensors provided information on the Martian atmosphere, surface composition, and thermophysical properties [*Kieffer et al.*, 1976; *Christensen*, 1982; *Presley and Christensen*, 1996]. For the past several years the Thermal Emission Spectrometer aboard the Mars Global Surveyor orbiter has collected hyperspectral TIR data that has been used to document the presence of primary rock-forming and secondary alteration minerals [*Bandfield et al.*, 2000a, 2000b; *Christensen et al.*, 1992, 2000a, 2000b]. The Thermal Emission Imaging System (THEMIS) on the Mars Odyssey orbiter will provide the highest spatial resolution (100 m/pixel) multispectral (10 bands between 6.5 and 14.5 μm) TIR data ever acquired at Mars [*Christensen et al.*, 1999]. The primary goals of the instrument are to determine the mineralogy and petrology of localized deposits and to study small-scale geologic processes using morphologic and thermophysical properties. At these resolutions, many small-scale geologic processes such as eolian and fluvial sediment transport, volcanic unit emplacement, and impact ejecta distribution can be examined in detail. However, tools such as the one described here will be needed to accurately map surface units, identify their constituent minerals, and trace their distribution from the source regions.

[7] This study described here was undertaken in order to extend previous laboratory validation of linear spectral deconvolution models [*Johnson et al.*, 1983; *Crown and Pieters*, 1987; *Eastes*, 1989; *Ramsey and Christensen*, 1998; *Feely and Christensen*, 1999; *Hamilton and Christensen*, 2000] into the regime of remotely acquired image data. Its purpose is twofold, however. Foremost was to choose a site for TIMS acquisition that would provide an excellent location to test the linear retrieval algorithm using image end-members rather than a priori knowledge from the laboratory. The criteria for site selection were (1) a location of known lithologic mixing in the semi-arid southwestern United States, (2) a site that posed a geologic question that could be addressed through the deconvolution analysis, and (3) a viable analog for future Mars TIR data. A secondary purpose was to understand the effects of resolution degradation on the retrieval algorithm, specifically as an analog to the upcoming 100 m/pixel THEMIS data. This phase of the study provides a baseline for assessing the errors one would expect if a similar analysis is carried out using lower resolution data such as THEMIS or ASTER.

[8] Using the aforementioned criteria, Meteor Crater, Arizona, was chosen for a TIMS overflight in the summer of 1994 (Figure 1). The semiarid environment, paucity of vegetation, and low relief make the region ideal for airborne, TIR data acquisition. The crater also fulfills all the desired prerequisites and, in addition, had an existing TIMS data line from 1987. Although the 1987 data contained significant noise and was not at the desired resolution, it enabled a precursory examination of the viability of the linear retrieval algorithm as a tool to separate lithologic image end-members in an earlier study [*Ramsey and Christensen*, 1992]. The choice of the crater as an analog for the small impact sites on Mars is obvious. However, previous scientific investigations had raised new questions as to the amount and style of erosion that had taken place on the crater ejecta deposit [*Schultz and Grant*, 1989; *Pilon et al.*, 1991; *Grant and Schultz*, 1989, 1993]. These studies used detailed field mapping, excavation, and ground-penetrating radar to determine the subsurface character of the ejecta blanket. Their findings revealed a much lower total vertical erosion (≈1–2 m) than the earlier estimates of 20–30 m [*Shoemaker*, 1960; *Shoemaker and Kieffer*, 1974; *Roddy*, 1978]. Because the amount and style of erosion of a crater's ejecta has a direct bearing on the local climatic and geologic history, the possibility of further constraining these rates with remote sensing becomes very important for upcoming Mars exploration. Further, impact craters excavate lithologies to a depth related to the size of the impacting body and therefore provide a window into the stratigraphy, which is not normally observed with orbital remote-sensing instruments. For all these reasons, Meteor Crater provides a unique target for testing the deconvolution model, the application of TIR remote sensing for determination of ejecta erosion, as well as an analog for multispectral TIR analysis of small craters on Mars.

2. Geology of Meteor Crater, Arizona

[9] Meteor Crater is located in north-central Arizona east of Canyon Diablo (Figure 1a). The current age estimate places the crater at approximately 50,000 years B.P. [*Nish-*

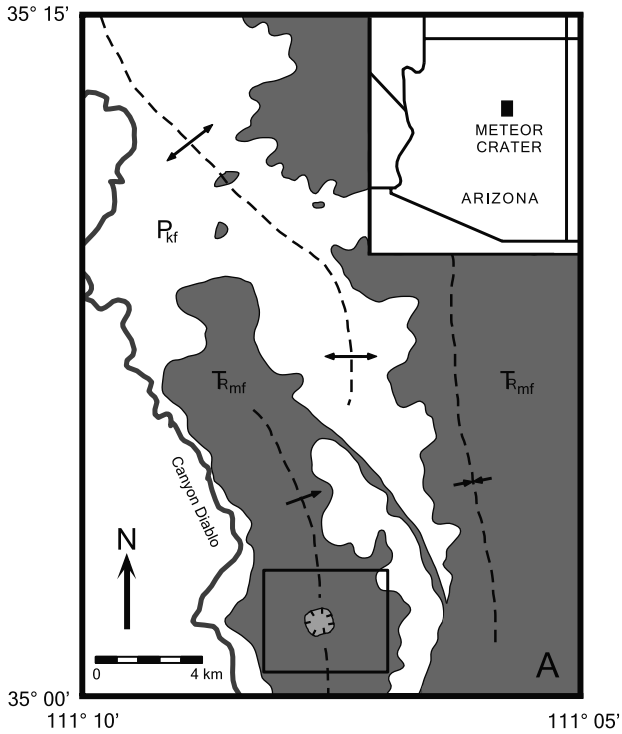

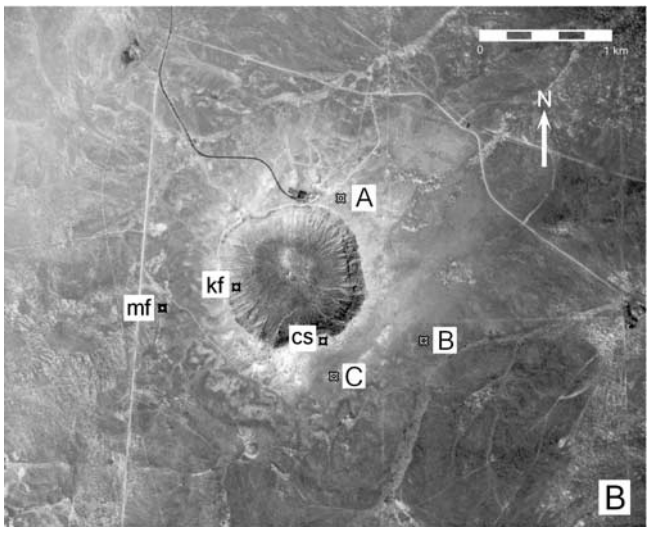

iizumi et al., 1991], making it one of the most recent and well-preserved impact sites on the planet. The impact of the iron meteorite produced a simple bowl-shaped crater that is approximately 180 m deep and 1200 m in diameter with a 30–60 m high rim. Early investigations of the site concentrated on determining the cause and finding the postulated buried meteorite [*Barringer*, 1905].

[10] The region of the southern Colorado Plateau where the crater is located is marked by numerous, small-scale monoclinal folds and wide-spaced, NW trending normal faults [*Shoemaker*, 1960]. These faults are traceable for many kilometers; however, the total vertical offset is only several meters or less. The dominant structural feature in the region, visible on air photos (Figure 1b) and responsible for the squarish appearance of the crater, are two mutually perpendicular, vertical joints sets [*Shoemaker and Kieffer*, 1974]. The NE-SW trending joints in conjunction with the slight NE regional dip (<5°) controls the trend of the secondary stream courses. Scissor faults occurring in the corners of the crater have resulted in nonuniform exposures of the strata on each of the four walls (Figure 2b). For example, the Coconino Sandstone is uplifted and exposed along portions of the north, east, and south walls, and remains lower, mantled by colluvium, along the western portion of the crater.

[11] Of the numerous, subhorizontal sedimentary units that form the upper Colorado Plateau, the deepest sampled by the impact event was the Permian Coconino Sandstone (P_{cs}), although only the uppermost Coconino Ss. is exposed in the crater walls. The sandstone exposed consists of fine-grained, cross-bedded quartz and is unusually clean [*McKee*, 1934]. A thin (≈3 m) bed of the Toroweap Formation conformably overlies the Coconino Ss. The Toroweap Fm. is a yellowish, coarse-grained dolomitic sandstone, and because of its limited exposure it is commonly grouped with the Coconino Ss. where mapping the ejecta [*Shoemaker and Kieffer*, 1974].

[12] Above the Toroweap Fm. lies the 80 m thick Permian Kaibab Formation (P_{kf}). Exposed within the crater are three distinct members (Alpha, Beta, and Gamma

Figure 1. (opposite) Location of Meteor Crater, Arizona, and image sample sites. (a) Regional geology of the Meteor Crater region of the Colorado Plateau (modified from *Shoemaker and Kieffer* [1974]). The area contains numerous small monoclinal folds, normal faults, and a dominant perpendicular NE-SW/NW-SE joint set (not shown on map). The Canyon Diablo region is also marked by a discontinuous, patchy veneer of Triassic Moenkopi Formation (TR_{mf}) eroding off the Permian Kaibab Formation. The Moenkopi Fm. is virtually nonexistent near the crater except for several erosional ridges. The boxed area indicates the approximate location shown in Figure 1b. (b) Aerial photograph taken in conjunction with the TIMS data acquisition. The presence of the regional joint set is responsible for the squarish outline of the crater. Bright primary ejecta within 1 crater radius consists primarily of Coconino Sandstone and Kaibab Formation. Eolian transport of these ejecta has formed the NE trending wind streak. End-member (cs, kf, mf) and mixed ejecta (A, B, C) sample locations for this study are indicated.

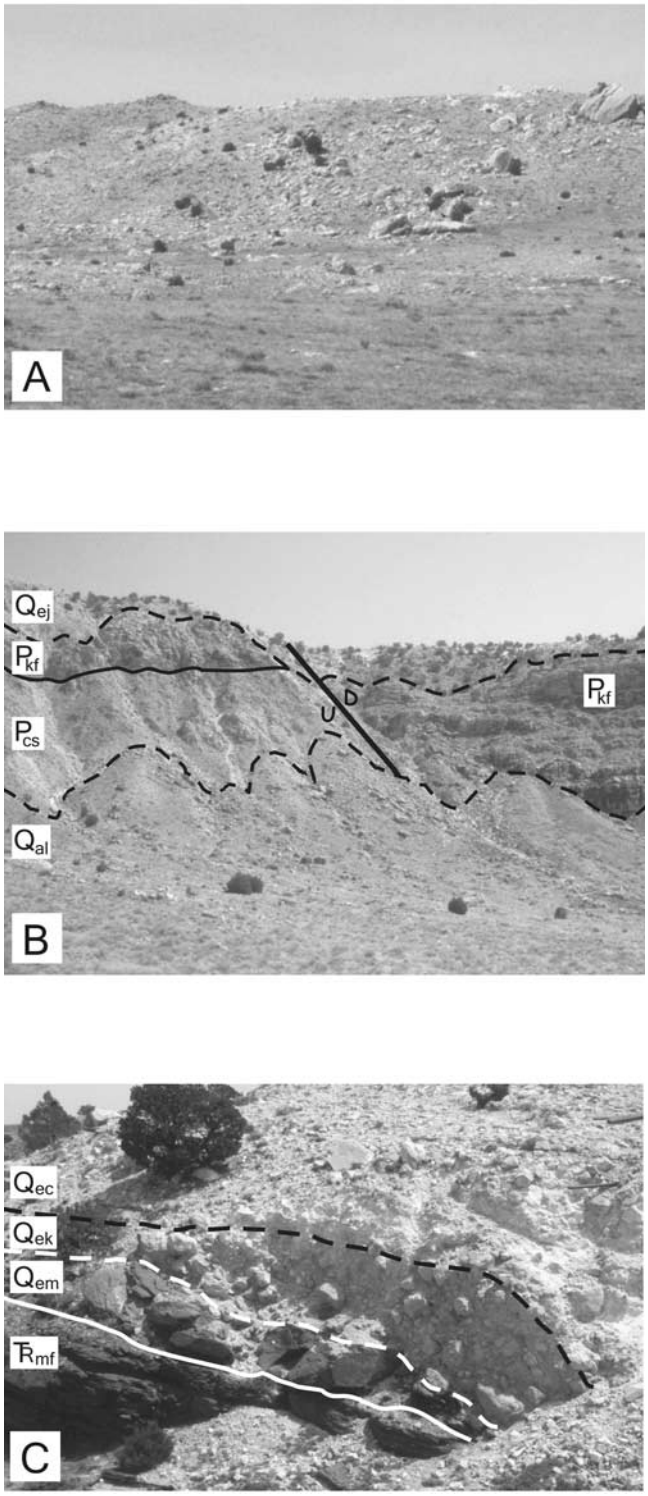

members) that are composed of fossfiliferous dolomitic limestone and minor calcareous sandstones, which are easily mapped in situ [*McKee*, 1938]. For example, the upper, Alpha member contains several thin sandstone interbeds that allowed *Shoemaker* [1960] to reconstruct the preimpact stratigraphic relationships of the units. However, the subtle mineralogical differences between these members of the Kaibab Fm. hindered attempts to separate them in the ejecta blanket using remote sensing alone, and therefore all members of the formation are treated as one unit in this study.

[13] The Kaibab Fm. is, in turn, covered disconformably by a thin (≈10 m), patchy veneer of the Triassic Moenkopi Formation (TR_{mf}). To the west of the crater, the Moenkopi Fm. has been completely eroded, exposing the upper surface of the Kaibab Fm. (Figure 1b). The Moenkopi Fm. exposed near the crater has two distinct members. The lower Wupatki member is a fine-grained, pale to light brown sandstone and rarely exceeds 1 m in thickness. The upper Moqui member is generally is 4–10 m thick and consists of dark reddish-brown fissile siltstones and crops-out as low ridges and buttes in the vicinity of the crater [*McKee*, 1954]. As in the case of the Kaibab Fm., the members of the Moenkopi Fm. have been averaged as 1 spectral unit in this study.

[14] These principal stratigraphic units are preserved in inverted order as primary ejecta up to 2 crater radii (≈1.2 km) away from the rim. This hummocky, near-rim ejecta consists of a continuous blanket formed by larger blocks ranging in size from 0.5–30 m (Figure 2a). The west, north, and eastern sides of the crater are dominated by Kaibab Fm. ejecta with several lobate deposits of Coconino Ss. interspersed. On the southern rim the vast majority of the deposit consists of Coconino Ss., which is easily discernible on aerial photographs (Figure 1b). Because of its friability and high porosity, this deposit supports a sparse stand of Pinon juniper trees and was the source for the majority of material that now comprises the northeast trending patchy wind streak. This deposit is a thin mantle that has been determined to be inactive from the superposition of 900-year-old basaltic ash from nearby Sunset Crater, the lack of bed forms, and the presence of vegetation [*Grant and Schultz*, 1993]. Although not determined, the onset of inactivity was likely caused by a change in the prevailing southwesterly winds [*Breed et al.*, 1984]. These winds may have persisted since crater formation; however, crater lake sediments indicate the climate has varied considerably in the past

Figure 2. (opposite) Field photographs of Meteor Crater. (a) View to the SW showing the near-rim blocky ejecta of the NE crater wall. Vegetation, accounting for 5–10% of the ground cover in this region, consists mainly of several species of desert grass and small cacti. (b) View from inside the crater looking SE at the exposed scissor fault. The eastern portion of the crater is uplifted exposing the underlying Coconino Ss. (see Figure 5). (c) South crater rim ejecta exposed in this view looking west. The inverted stratigraphy is clearly exposed with the ejecta of the Coconino Ss. (Q_{ec}), Kaibab Fm. (Q_{ek}), and Moenkopi Fm. (Q_{em}) units overlying the in situ Moenkopi Fm. (TR_{mf}).

[*Forester*, 1987]. Because the regional climate has been nearly uniform since the Holocene, the wind streak likely dates back to at least 8–10 ka [*Nishiizumi et al.*, 1991; *Grant and Schultz*, 1993].

[15] Holocene alluvium surrounding the crater consists of fragments from each of the ejecta units. Much of it is derived from the small fans that have been deposited by the numerous radial gullies incised around the crater rim. This reworked material has been transported by the diffuse drainages to the east and northeast, mantling the outer continuous ejecta blanket. To the west and southwest, the character of the hummocky ejecta is considerably more muted than the rest of the crater rim. *Garvin et al.* [1989] noticed this change using airborne laser altimetry (ALA) and attributed it to the lessening of the crater slope due to eolian burial by fines transported from the southwest.

[16] Within the crater, the uppermost floor deposits are formed from trapped airborne dust and basaltic ash from the nearby San Francisco volcanic field. Below these surficial deposits, drill cores reveal 30 m of interfingered Quaternary lake beds and alluvium overlying approximately 10 m of mixed breccia [*Shoemaker and Kieffer*, 1974]. This unit contains the most strongly shocked host rock and highly oxidized meteoritic material found at the crater. The zone extending from the base of the mixed breccia to 200 m contains impact melt and fine spherules of meteoritic material [*Barringer*, 1905; *Shoemaker*, 1960]. Gravity and magnetic surveys placed the depth of the fractured bedrock at 225 m below the surface of the crater floor [*Regan and Hinze*, 1975].

[17] The early search for a hypothesized iron ore meteorite at Meteor Crater has given way to important scientific studies of crater formation, ejecta deposition, and later erosion [*Shoemaker*, 1960; *Roddy*, 1978]. On the basis of the apparent lack of mapped ejecta from units such as the Coconino Ss., these studies reported 20–30 m of vertical erosion had occurred in the near-rim vicinity (600 m). However, more recent investigations have concentrated on the plains farther out. Using ground-penetrating radar [*Pilon et al.*, 1991], and trenching and sieve analysis [*Grant and Schultz*, 1989, 1991], the total erosion has been estimated at no more than 1–2 m. On the basis of these results, *Grant and Schultz* [1993] reinforce their argument of low erosion by citing the apparent lack of reworked Coconino Ss. in the surrounding depositional traps. It would be assumed that detectable volumes of reworked Coconino Ss. should be present in these traps if the crater rim had been eroded by more than 20 m, unless this eroded material had already been removed entirely from region.

3. Methodology

3.1. TIMS Data Acquisition and Processing

[18] The TIMS instrument is a cross-track, six-band imaging scanner that records emitted thermal energy within the 8–12 μm region of the electromagnetic spectrum. This window in Earth's atmosphere is relatively free from absorption and scattering that dominate the wavelengths on either side of the window. The radiant energy detected by the instrument is calibrated using two internal blackbodies and is stored on tape. A detailed description of the TIMS instrument operation, data products, and general processing routines is given by *Kahle and Goetz* [1983] and *Palluconi and Meeks* [1985].

[19] The measured energy is a function of the temperature and emissivity of the surface but contains a component from the scattering, absorption, and emission within the atmospheric path between the scanner and the ground. This atmospheric energy is greater at the image edges, where the atmospheric path is 22% longer, as well as in TIMS bands 1 and 6, which are both on the periphery of the atmospheric window. Correction by removal of the atmospheric term can be accomplished in several ways [*Barbera*, 1989; *Edgett and Anderson*, 1995; *Berke et al.*, 1989]; however; for this study the path radiance was removed using the MODTRAN radiative transfer model [*Berke et al.*, 1989].

[20] As a result of the cross-track scanning motion of the TIMS instrument, the image swath width appears compressed. Correction for this geometric distortion is easily accomplished but requires resampling the data from nadir to the image edge. The increased atmospheric and geometric corrections necessary on the image edges generally preclude these portions of the data during further detailed spectral examination. However, if included, these areas commonly contain higher errors, which must be factored into the final interpretations.

[21] The atmospherically, geometrically, and radiometrically corrected radiant energy in each TIMS pixel is solely a function of the surface emissivity in each wavelength band and the temperature of the ground surface. However, in order to determine the emissivity and derive the temperature uniquely for any given pixel, an underdetermined system of equations must be solved. For example, the TIMS images the surface over six wavelengths and therefore records six radiance values per pixel, which contain the six emissivity values plus the surface kinetic temperature. The determination of these seven unknowns must be done by making an assumption about either one of the emissivity values or the temperature, or by introducing extra data such as laboratory-derived spectra [*Kahle*, 1987; *Realmuto*, 1990; *Hook et al.*, 1992]. Of the various permutations on separation of emissivity from temperature, typically the most straightforward (and the one used for this analysis) is the normalized emittance technique similar to that described by *Christensen* [1982] and *Realmuto* [1990]. The basic premise of the model is the assumption of a maximum emissivity value (ε_{max}) at or near unity, although the wavelength of this maximum is not specified. *Realmuto* [1990] found maximum emissivity values ranged from 0.95 to 0.99 for quartzite and basalt, respectively. A more detailed examination by *Salisbury and D'Aria* [1992] of over 60 samples spanning all compositions and rock types found an average ε_{max} of 0.983 ± 0.002. An underprediction of the actual emissivity will result in a higher temperature for that pixel and slight distortion of the derived emissivity spectrum in the remaining bands. However, an uncertainty in the ε_{max} of ± 0.05 resulted in a kinetic temperature error of only 3 K (at 10 μm and 300 K) and a change in the derived spectral shape that produced <0.5% error in the final deconvolution end-member results [*Ramsey and Fink*, 1994]. On the basis of these results and in comparison with laboratory spectra of samples collected during field mapping, a value of 0.985

Table 1. TIMS 1994 Data Acquisition for Meteor Crater, Arizona

Flight Line	Orientation	Altitude, m above ground level	Spatial Resolution, m
1	E-W	1219	3.2
2	W-E	2194	5.5
3	E-W	4267	10.9

was chosen for this study. This value was used to solve for the maximum kinetic temperature (T_{max}) and the remaining five unknown emissivity values. The pixels of the emissivity images produced by this approach form the unknown or mixed spectra that are deconvolved using the least squares model.

3.2. Constrained, Least Squares Deconvolution Model

[22] The assumption that the unknown spectrum is a linear combination of certain reference or end-member spectra allows for a relatively simple statistical determination of the best fit end-member percentages for a given mixed spectrum [*Adams et al.*, 1986; *Sabol et al.*, 1992; *Ramsey and Christensen*, 1998]. Using the notation and approach of *Ramsey and Christensen* [1998] and assuming that the emissivity data are normally distributed, the solution to any mixed pixel in the scene is a minimization of the square of difference between the measured and modeled emissivity values, divided by the standard deviation of each value [*Ramsey*, 1996]. Therefore, assuming that each ejecta spectrum is a mixture of the spectra from the three lithologic end-members, the mathematical expression for that mixture is stated by the following equation and constraint,

$$\varepsilon(\lambda)_{\text{ejecta}} = \sum_{i=1}^{3} \left[\zeta_i \varepsilon(\lambda)_i\right] + \delta(\lambda) \qquad \zeta_i = 1.0 \qquad (1)$$

where ζ_i is the fractional percentage of the *i*th end-member and $\delta(\lambda)$ is the residual error at each wavelength. Using the three end-members for Meteor Crater, any given TIMS pixel can be expressed using (equation (1)) expanded to

$$\varepsilon(\lambda)_{\text{ejecta}} = \left[\zeta_{cs}\varepsilon(\lambda)_{cs} + \zeta_{\text{kf}}\varepsilon(\lambda)_{\text{kf}} + \zeta_{\text{mf}}\varepsilon(\lambda)_{\text{mf}}\right] + \delta(\lambda)\,; \quad \left[\zeta_{cs} + \zeta_{\text{kf}} + \zeta_{\text{mf}}\right] = 1.0. \qquad (2)$$

[23] The choice of end-members is arbitrary depending on the desired study. End-members can either be selected directly from the image (as is the case for this study), with the knowledge that these may or may not be spectrally pure, or derived from a library formed from field and/or laboratory spectra [*Christensen et al.*, 2000c]. The number of end-members chosen is also arbitrary; however, it must be less than or equal to the number of instrument channels. *Gillespie et al.* [1990a] have shown that three or four end-members, the number of principal components exceeding the noise level of a typical TIMS image, can accurately represent a scene.

[24] For the six bands of the TIMS instrument and the three end-members used here, the root mean squared (RMS) error, which determines the "goodness of fit" of the model, is related to the residual error term through the following equation:

$$\text{RMS} = \sqrt{\frac{\sum_{j=1}^{6} \delta(\lambda)_j^2}{6}} \qquad (3)$$

The RMS error is particularly useful for the TIMS analysis where it is displayed in an image format, spatially indicating regions of poor model fit. These regions may indicate an unmodeled end-member, nonlinear mixing, or some other complicating effect. The remaining portion of the image is considered to have an acceptable fit where the values of the RMS error have an absolute emissivity variation of <0.5% [*Gillespie et al.*, 1990b; *Ramsey and Christensen*, 1998].

3.3. Meteor Crater TIMS Data

[25] Thermal infrared multispectral scanner data for Meteor Crater, Arizona, were acquired at 1230 LT on 22 August 1994. The data were collected by the NASA C-130 aircraft that carried an additional payload of two infrared cameras and a visible/near-infrared scanner that simulated the Landsat TM channels. To study the effects of variable resolution on the deconvolution analysis, data were collected at multiple altitudes (Table 1). At the time of the overflight, visibility was >100 km with sparse clouds (<5%) and low humidity (<15%). During atmospheric correction the mid-latitude summer profile of the MODTRAN model was used; however, very little correction was necessary because of the favorable atmospheric conditions. These minimal corrections, coupled with the fact that the crater and primary ejecta were generally centered in the images, allowed the edges to be included in all further analyses, noting the slightly higher errors as previously mentioned in section 3.1.

[26] The image-derived spectra of the three principle stratigraphic units (Moenkopi Fm., Kaibab Fm., and Coconino Ss.) were chosen as end-members for the data (Figure 3). The location of each of the end-members

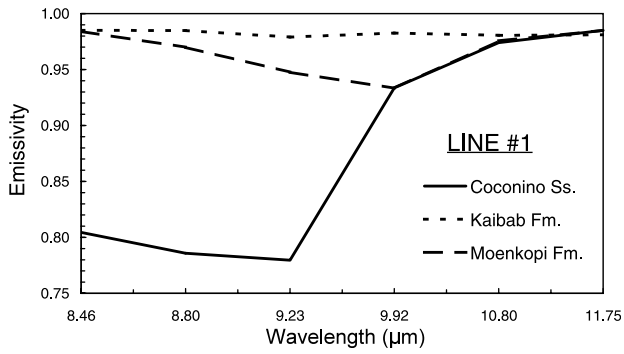

Figure 3. TIMS-derived surface emissivity spectra of the lithologic end-members derived from flight line 1 (3.2 m/pixel spatial resolution). The relative featureless spectra of the Kaibab Fm. is characteristic of most carbonates, with the slight low in band 3 indicative of a minor quartz contamination, whereas the large absorption band of the Coconino Ss. spectrum is similar to that of nearly pure quartz. The Moenkopi Fm. has a dominant illite fraction, which, in conjunction with the presence of quartz, is responsible for the smaller feature shifted to longer wavelengths.

(Figure 1b) was based on knowledge of rock outcrops from field mapping and the strength of the spectral features observed in the processed emissivity data. The choice of rock units, rather than minerals, was made for several reasons. The primary objective of this research was to determine the limits of the deconvolution model using image-derived spectra at various spatial resolutions (Figure 4). Further, the scientific question at the crater centers around erosion of the lithologic units, not the primary minerals that comprise them. Previous workers have mapped these deposits in terms of their stratigraphic units, and therefore the results of this analysis can then be directly related to the previous results. Finally, these three units have considerable mineralogic variability, making their spectra easily differentiated by the retrieval algorithm.

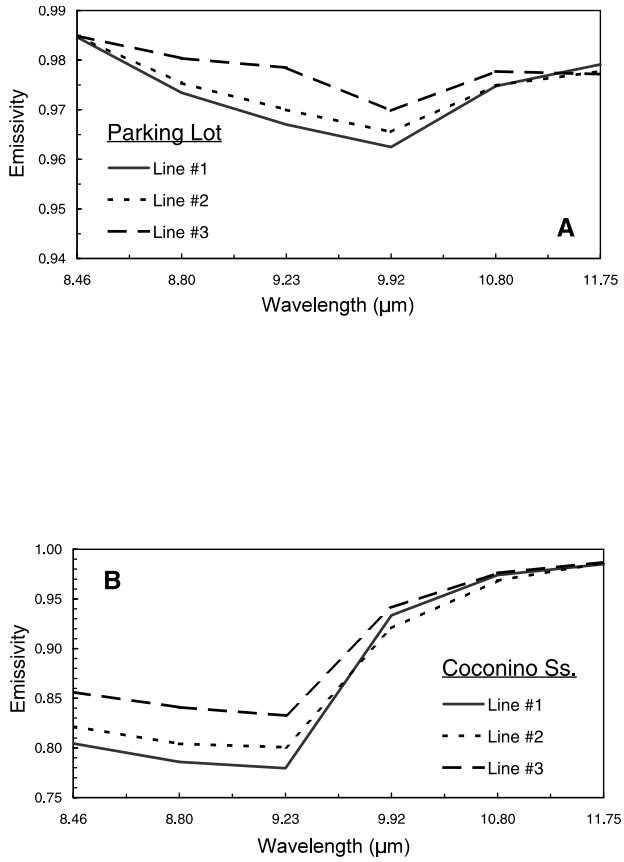

Figure 4. Variations in emissivity spectra upon spatial resolution degradation. (a) Calibration target-visitor center parking lot spectra averaged from over 20 pixels. The spectra show less than a 0.2% deviation between the low-altitude and midaltitude flights. Line 3 has the largest contrast with a 1.1% emissivity variation at 9.2 μm, which is likely due to the longer atmospheric path length and incomplete correction for atmospheric ozone. In order to compensate for these variations and compare the data sets, emissivity images from lines 2 and 3 were adjusted slightly by the differences from line 1 in the parking lot spectra. (b) Coconino Ss. spectra showing a significant shallowing of the quartz feature with lower spatial resolution. This is due to mixing with emitted energy from either the Kaibab Fm. and/or vegetation surrounding the end-member site. The line 2 spectrum also contains a slightly lower emissivity at 9.9 μm due to the addition of emitted energy from the Moenkopi Fm. which contains a dominant absorption band in this region.

4. Results

4.1. Line 1 Image Analysis

[27] The end-member images are output from the model with a digital number (DN) scale ranging from 0 to 100 (0–100% of the end-member) and indicate distinct patterns within the ejecta. In order to provide better discrimination in the end-member images, all figures were linearly stretched to a range of 0–255 DN. Figure 5 shows the Coconino Ss. end-member for line 1 and clearly reveals several features in and around the crater. The most highly concentrated region of Coconino Ss. is the ejecta flap to the south. It is this area that provides the source deposit for the NE trending wind streak. The quartz-rich material comprises the uppermost layer of the wind streak and is visible up to 5 crater radii (3 km) to the northeast, with strong (>30%) concentrations as far out as 1 km. This is contradictory to *Grant and Schultz* [1993], who only found primary or reworked Coconino Ss. ejecta within 0.5 crater radii. One explanation is that the reworked ejecta comprising the wind streak are not strongly concentrated and consisting of sand-sized grains (<300 μm), thereby making it hard to distinguish from the sediments derived from the other units. This was confirmed during field examination of the ejecta deposits related to this work. To the north and northeast of the crater, the Coconino Ss. crops out in large ejecta blocks that also serve as source locales for eolian-transported material. The bedding, visible only along the northern and eastern crater walls, indicates the displacement of the stratigraphy due to the scissor faults occurring in the crater corners (Figure 2b). In the northeastern half of the crater the units have been displaced upward relative to the southwest where the Coconino Ss. is not exposed at all.

4.2. Resolution Degradation

[28] The Meteor Crater visitor center/museum parking lot was chosen as a calibration target because if its known spectral signature and large size (which provides the ability to accurately choose pixels with little to no spectral contamination as the resolution was degraded by 300%). Despite each altitude data set being processed equally, minor variations of emissivity occurred over this target. For any location within the image these deviations are typically less than 1.5% and are caused by errors in atmospheric removal, the movement of that region within the TIMS scene when viewed at different altitudes, and changes in instrument conditions such as air temperature and scan speeds. These emissivity differences among the three data sets were corrected through a first-order approximation by comparing the averaged spectra of the parking lot (Figure 4a). The asphalt emissivity spectra of the mid- and high-altitude lines were fit to that of the low-altitude line (1219 m), which is assumed to be the most accurate. Under the operating conditions at 1219 m, the TIMS internal blackbodies were subject to the warmest ambient air temperature and acquired energy that had the least amount of atmospheric path radiance. The major emissivity

Figure 5. Line 1 end-member image of the Coconino Ss. with the lighter areas indicating a higher end-member percentage. Clearly visible are the ejecta flap to south of the crater and the sandstone cropping out along the eastern crater wall (see Figure 2b). The southern flap is the primary source for the wind streak extending to the northeast. Several larger ejecta blocks are also visible to the NE of the crater rim.

variation occurred at the highest altitude, with a maximum difference in band 3 of 1.1%. By correcting the data through this type of first order approach, subsequent model results derived from different altitudes are assured to be due to factors other than instrument and atmospheric changes.

[29] The end-member sites located in Figure 1 were identified in lines 2 and 3, and their spectra were extracted. These spectra have very similar morphologies where compared with those from line 1. The most significant difference, however, is the marked shallowing of the Coconino Ss. spectrum (Figure 4b) and, to lesser extent, a deepening of the Kaibab Fm. and shallowing of the Moenkopi Fm. spectra by $\sim$1% in bands 2, 3, and 4, respectively. The observed changes in spectral contrast with spatial resolution degradation result from the contamination of end-member radiance with the radiance from neighboring pixels. The minimal change in the spectra of the later two units attests to the large areal extent of their outcrops, whereas the Coconino Ss. spectrum, taken from the southern ejecta flap, clearly integrated some percentage of Kaibab Fm. and/or vegetation as the pixel size increased. Similarly, by incorporating a larger area, the pixels that comprised the Kaibab Fm. end-member in line 3 came to include some amount of energy from the overlying Moenkopi Fm. rocks. Mixing such as this occurs at all scales down to the mineral grain level, and the choice of what constitutes a spectral end-member will have an effect on the results of the linear retrieval algorithm.

[30] As mentioned, the major variation from the end-member spectra derived from line 1 and those from line 2, the median altitude flight, occurs in the Coconino Sandstone. The spectrum displays clear contamination from the Kaibab Fm., and, as a result, ejecta patterns in the images are slightly different. Even with this mixed component, the primary ejecta patterns mentioned in section 4.1 are still well defined. In fact, with the expanded swath width, the wind streak is now traceable extending some 5 crater radii away.

4.3. Lines 2 and 3 Image Analyses

[31] The Kaibab Fm. end-member image (Figures 6b and 7) has a greater overall percentage throughout the scene than other end-members. Much of this higher average is caused by the complicating presence of eolian-reworked, spectrally flat, fine-grained material (dust); vegetation; and the exposed Kaibab Fm. itself where the Moenkopi Fm. has been eroded. The strongest occurrences of the Kaibab Fm. end-member pixels are along the crater walls and throughout most of the floor, as well as the hummocky, near-rim ejecta. The blocky ejecta is strongly concentrated around the entire crater rim, except for the south where it is mantled by Coconino Ss., and extends out to slightly greater than 1 crater radius. Blocks of this material appear coherent in the field with only minor spalling and degradation and therefore do not contribute significantly to the generation of eolian-reworked deposits in the wind streak. The Kaibab Fm., however, does form the primary component of the surrounding ejecta blanket. This ejecta consists chiefly of a rubble lag deposit [*Grant and Schultz*, 1993] and is visible mantling dark regions (exposed in situ Moenkopi Fm.) to the west (Figure 6b). Because of the spectral similarity of limestone, dust, and vegetation in the TIMS 6-point spectra, it is assumed that a small percentage of the Kaibab Fm. end-member in the images is due to spectral contamination of the vegetation cover and fine-grained dust. The uniform distribution of the vegetation throughout the scene makes this slight overprediction insignificant.

[32] Finally, the Moenkopi Fm. end-member images (Figures 6c and 7) show much fewer exposed end-member pixels than the previous units, consistent with field mapping. The most concentrated Moenkopi Fm. outcrops occur where discontinuous patches of the flat-lying bedding plane are exposed west of the crater, along the extreme upper edge

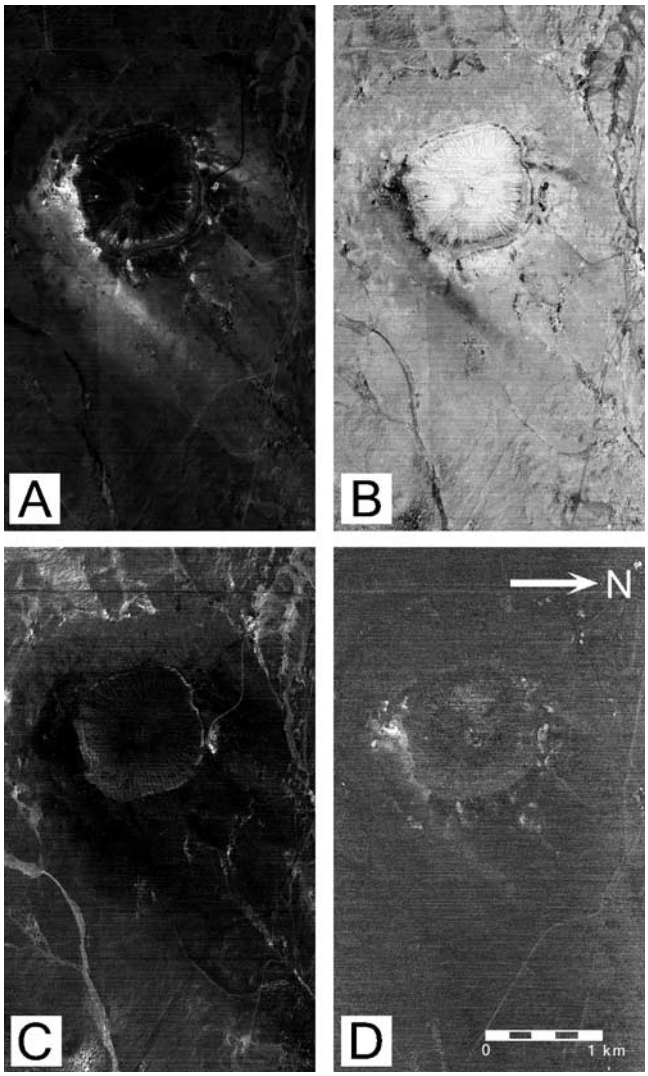

Figure 6. Line 2 end-member images. (a) Coconino Ss. end-member showing similar patterns to those in Figure 5. With the larger swath width, the nearly full extent of the patchy wind streak is visible. This eolian reworked material occurs up to 5 crater radii from the crater rim. (b) The Kaibab Fm. end-member, in comparison to that of the Coconino Ss., more uniformly distributed throughout the scene. The strongest occurrences are along the crater walls and bottom, and the near-rim blocky ejecta. (c) The Moenkopi Fm. occurring along the upper rim of the crater, concentrated in the diffuse drainages, and as a mantling of the dominantly Kaibab Fm. ejecta blanket to the west. The current extent of the primary ejecta blanket, marked by the dark halo surrounding the crater in this image, is also evident. (d) Highly stretched RMS error image with the brightest pixels indicating regions of poor model fit. The relative lack of topography and recognizable features indicate that the primary errors were confined to atmospheric and instrument noise. The strongest errors occur over portions of the southern ejecta flap and western crater wall (see text). These regions have spectral features that fall outside the emissivity area defined by the end-members and therefore are not fit well. Average scene RMS error was 0.24%, indicating a good model fit to the data.

of the crater rim, and in washes and minor ridge outcrops to the east and northwest. A much more subtle pattern, but significant to the question of the volume of eroded ejecta, is the encroachment of Moenkopi Fm. over the western edge of the primary Kaibab Fm. eject blanket. The dominant SW winds responsible for the wind streak also appear to be transporting material from the west, mantling the hummocky ejecta. This result is consistent with *Garvin et al.* [1989], who used ALA and found that this portion of the ejecta blanket had a gentler slope with a lower power law function (radial decay of thickness) than the rest of the crater ejecta. The discontinuous exposures of the Moenkopi Fm. along the northeast crater rim also coincide with the detailed crater geologic map of *Shoemaker* [1960] and *Shoemaker and Kieffer* [1974]. The absence of the Moenkopi Fm. along portions of the rim is due to thrust faults with displacements of several meters. The images also reveal a distinct dark halo around the crater. This halo or "end-member lacking" zone is an indicator of the approximate extent of the primary ejecta blanket still present. The halo extends for slightly more than 1 crater radius and is

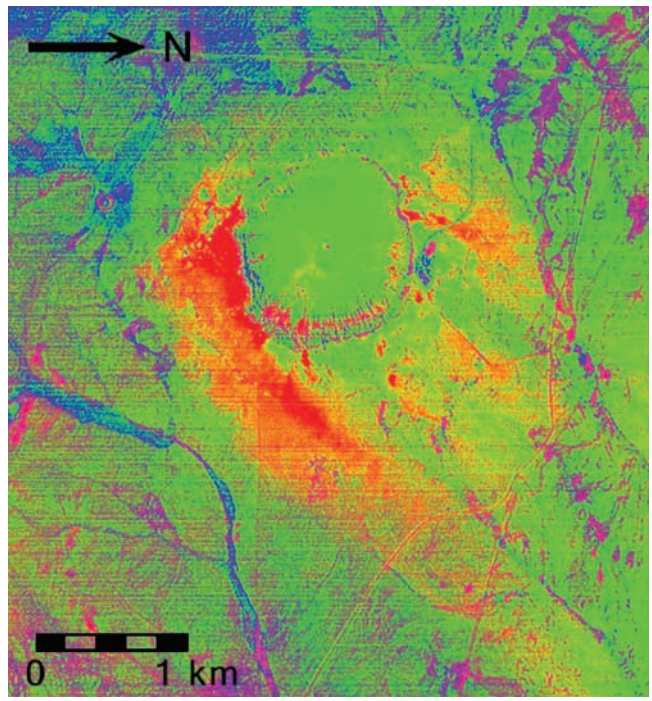

Figure 7. Color composite of the end-members derived from the line 3 data set, with the Coconino Ss. image in red, the Kaibab Fm. image in green, and the Moenkopi Fm. in blue. The Coconino Ss. dominated wind streak is easily discriminated up to 5 crater radii to the NE, appearing reddish-yellow where mixed with the Kaibab Fm. The crater floor consists primarily of Kaibab Fm. as does the surrounding region, where exposed by the erosion of the overlying Moenkopi Fm. To the NW of the visitor center parking lot the Moqui member of the Moenkopi Fm. has not been eroded and forms a low ridge that is highlighted in magenta. The quartz of the Moqui siltstone is more dominant and therefore shows as a mixture of blue and red (Moenkopi Fm. plus Coconino Ss.).

much more expansive than that mapped by *Shoemaker and Kieffer* [1974].

4.4. Extrapolation to THEMIS Resolution

[33] The work performed herein provides an excellent starting point from which to extrapolate to the scale of the THEMIS spatial resolution and provide some insight into the expected errors of a similar analysis on Mars. The TIMS data were degraded from 3.2 to 100 m/pixel, and the deconvolution model was rerun with results for the Coconino Ss. end-member shown in Figure 8 (compare with Figure 5). As expected, the end-member image no longer shows the small-scale detail or the layering within the crater walls. However, it clearly does show the dominant wind streak and high end-member concentration throughout. This indicates that deconvolution at the 100 m scale (assuming the spectral contrast between end-members is significant) allows for simple visual identification. A more quantitative analysis was also performed, comparing the deconvolution results for the three, randomly selected sites in the scene. Figure 9b displays the results for the Coconino Ss. end-member at each of the three resolutions obtained by TIMS as well as extrapolated to THEMIS resolution. Significant variation (10–20%) in the model results occurred as the resolution was degraded from 3.2 to 100 m/pixel. The pixel averaging caused spectral mixing and was the most pronounced at sites A and B, which have higher percentages of the more subdued spectral end-members. This initial study does not categorically define the THEMIS potential, but it does indicate that caution should be applied when deconvolving THEMIS data using image/lithologic end-members. Discrimination of units is clearly possible, but precise determination of surface percentages to better than 15% may be difficult at the 100 m/pixel spatial resolution.

4.5. Coconino Ss. Ejecta Estimate

[34] The volume of Coconino Sandstone ejected versus that which remains has been used to argue the degree of erosion experienced at the crater. Reasonable theoretical bounding estimates (Table 2) can be made on the basis of known cratering scaling laws [*Roddy*, 1978; *Croft*, 1980]. However, the volume that is still present after 50,000 years remains in question because it has direct bearing on the rate and style of erosion at Meteor Crater. Lower estimates would imply a greater degree of erosion and subsequent removal of the unit from the area. Because of the paucity of visible primary ejecta in the near-rim region, *Shoemaker* [1960] and *Roddy* [1978] invoked 20–30 m of erosion, thereby removing most the Coconino Ss.

[35] *Grant and Schultz* [1993], on the other hand, list several convincing arguments stating why only 1–2 m of erosion has taken place. They state that near-rim exposures occur at elevations lower than adjacent alluvial terraces and yet are not mantled by material. In addition, interfluve areas around the crater rim remain untouched by erosion, indicating only incipient fluvial erosion. Further, they argue that the lack of appreciable concentrations of the Coconino Ss. throughout the region precludes its initial widespread occurrence. Finally, the total volume of ejected sandstone (Table 2) needed to account for 20 m of erosion exceeds the maximum calculated based on theoretical modeling.

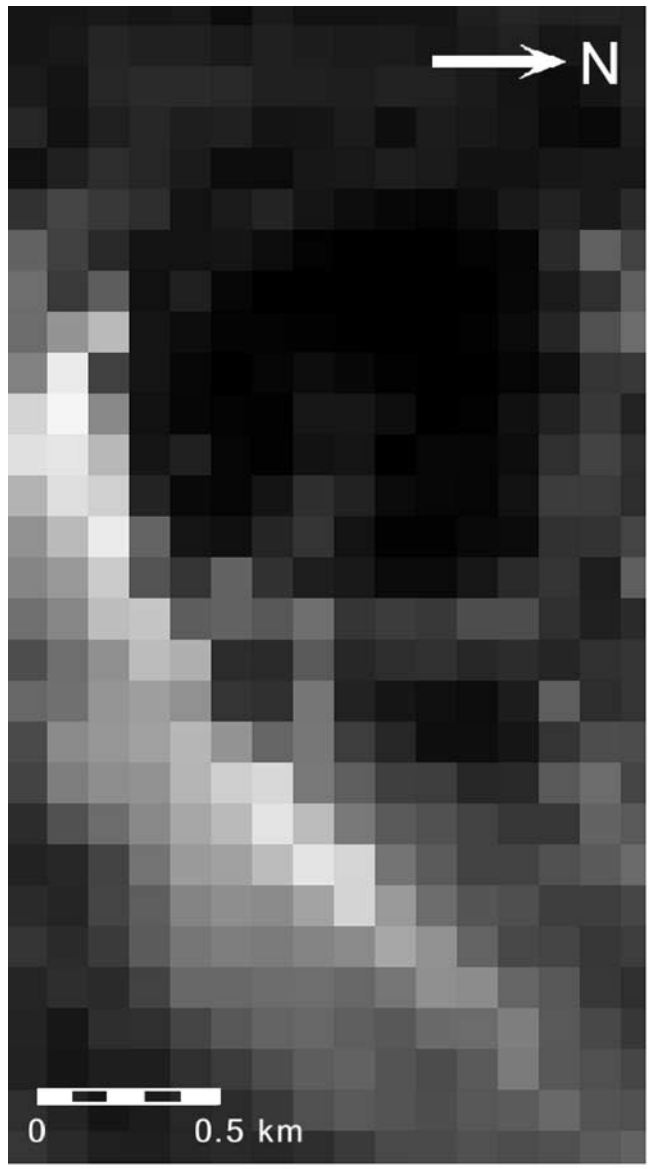

Figure 8. Modified Coconino Ss. image (see Figure 5) derived from TIMS data that were degraded to THEMIS resolution (100 m/pixel) prior to application of the deconvolution model. At this lower spatial resolution the NE trending wind streak is still visible as is the subtle patterns in the crater wall and floor. This reinforces the potential that possible stratigraphic variations exposed in crater walls on Mars should be identified with THEMIS if their spectral variations are significant.

[36] The amount, location, and distribution of the Coconino Ss. ejecta have been especially important in arguments for the total erosion at the crater. The basic product of the retrieval algorithm is the end-member image, which shows the areal extent, sources, and mixing patterns of that end-member. Given the areal extent of the ejecta deposits, together with estimates of the thickness of these deposits derived from geological and geophysical field investigations, an estimate of the volume of Coconino Sandstone ejected can be made.

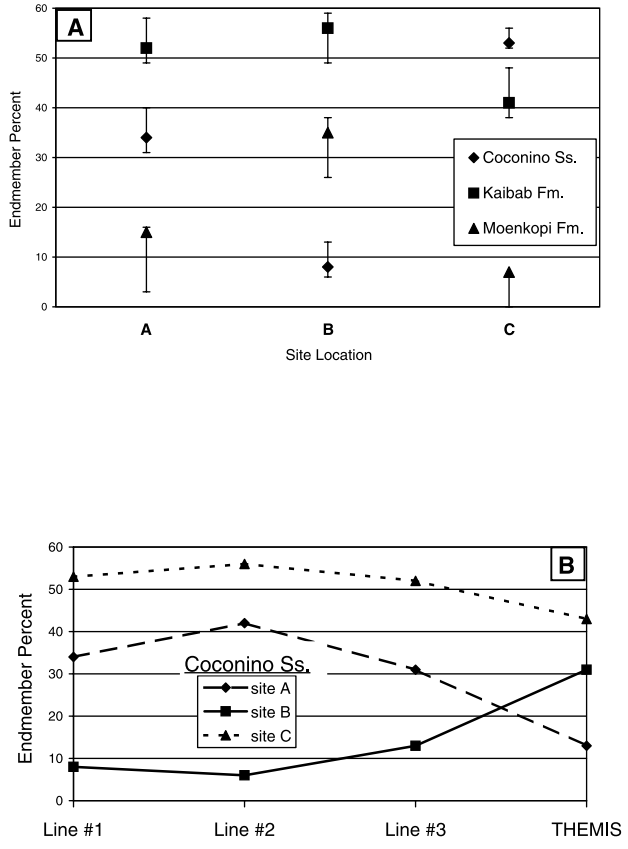

Figure 9. Variations in the model-predicted results with degradation of the image resolution. (a) Model-predicted percentages as a function of image resolution for locations A, B, and C shown in Figure 1b. The plotted values are the results from line 1, and the error bars indicate the maximum variation of the model with changes in the spatial resolution. These locations were randomly chosen throughout the ejecta blanket and wind streak. All three have appreciable amounts of each end-member; however, the largest deviations occur in the Moenkopi Fm., which had the lowest modeled percent of the three sites. Resolution errors vary from 1 to 15% with an average equal to 5.8%. This value indicates a linear relationship as a function of the approximately 6% change in spectral contrast of the sandstone end-member spectra due to the increased pixel size. (b) Changes in the predicted Coconino Ss. percentages for each sample site (A, B, C) as a function of resolution degradation. Site C shows the least variation because it is surrounded by high Coconino Ss. (the southern ejecta flap); it contains the highest percentage of Coconino Ss. end-member initially; and the sandstone also has the largest spectral variation of the three end-members. Variations of more than 20% at the other sites, which contain higher percentages of the more subdued spectral end-members, occur where resolution is degraded to 100 m/pixel (THEMIS).

[37] This strategy was applied to the line 2 Coconino Ss. end-member image. This line was chosen because it provided a reasonable compromise between areal coverage and pixel resolution. An image mask was applied in order to disregard pixels within the crater, parts of the visitor center, and regions far from the crater and ejecta. Only Coconino Ss. pixels directly comprising the primary ejecta and wind streak were counted. This end-member percentage summation where multiplied by the pixel resolution resulted in the total areal coverage. To derive a volume based on the linear retrieval results (Table 2), two bounding ejecta thickness values were chosen (100 μm and 5 m). These values represent the depth of maximum penetration of TIR energy and the average total thickness for the near-rim ejecta derived by *Pilon et al.* [1991] by ground-penetrating radar. The results of such a calculation are based on several assumptions. The most significant of these is that Coconino Ss. ejecta is not buried below pixels that show a 0% model-predicted value in the end-member image, in which case it would be undetectable using remote sensing. Second, it is assumed that the end-member percentage derived from the model for any given pixel remains constant with depth. In other words, ejecta from the other units underlies the exposures on the surface in the same percentage.

[38] The first assumption is at the center of the erosion question at the crater, and short of total excavation of the ejecta blanket, no accurate estimate can be made concerning a value of unexposed Coconino Ss. However, on the basis of the lack of sandstone exposure in the western crater wall, and the results of drainage excavations on the western ejecta blanket by *Grant and Schultz* [1993], it appears that there is little, if any, Coconino Ss. in this region. The areal extent of the wind streak throughout the rest of the scene assures that much of the remaining ejecta blanket will be included in the analysis. Finally, the second assumption will increase in error with depth. During deposition of the ejected material, some mixing of the lithologic units certainly took place. However, because crater formation deposits the units in inverted stratigraphic order, it is likely that Coconino Sandstone ejecta would disappear at some depth in the ejecta blanket. Clearly, there is Kaibab Fm. and Moenkopi Fm. ejecta below the surface exposures of Coconino Ss.; however, the depth and percentage of each is unknown. As a reasonable upper bound estimate, the percentage of Coconino Ss. present at depth was assumed to be similar to the surface exposure determined by the model.

[39] The minimum value of existing Coconino Ss. calculated using a depth of 100 μm clearly underestimates the smallest predicted volume of excavated sandstone [*Croft*, 1980], whereas the maximum value using 5 m depth overestimates the largest theoretical volume [*Roddy*, 1978]. If, in fact, the Coconino Ss. is only a 100 μm veneer over the entire wind streak, then much of the original ejecta would have to be assumed to be eroded. This depth estimate may be true for much of the far-rim wind streak, but it is clearly inaccurate for the large near-rim ejecta flap to the south of the crater, where exposures 1–2 m are observed (Figure 2c). Similarly, the value of 5 m used here to estimate the Coconino Ss. ejecta volume is exaggerated because of the presence of the other units comprising the ejecta flap and

Table 2. Estimated Volume of Coconino Sandstone[a]

Source	Minimum, m^3	Maximum, m^3	Comments
Roddy [1978]	ND	26.0×10^6	Total volume excavated
Croft [1980]	11.0×10^6	ND	Total volume excavated
This work	0.18×10^6	87.4×10^6	Total volume remaining

[a] ND is not determined.

the gradual thinning of the blanket with distance, and especially considering that volume is 3 times larger than maximum theoretically derived amount. The more likely estimate would place the Coconino Ss. volume somewhere between that of *Croft* [1980] and *Roddy* [1978] (Table 2). For example, choosing a median value of 15×10^6 m^3 and using the areal percentages derived from the retrieval algorithm would result in an average uniform depth of 85 cm. Using this approach with the theoretical maximum excavated volume proposed by *Roddy* [1978] only results in an average thickness of 1.47 m. Clearly, there is a decay with distance in the thickness of the Coconino Ss. from several meters near-rim to perhaps only microns at the distal edge of the wind streak. The estimates of meter-scale thickness are consistent with the field and theoretical data and agrees with the values of *Grant and Schultz* [1993] and *Grieve and Garvin* [1984], and are far less than the original 20–30 m amount of *Shoemaker* [1960].

[40] On the basis of these results, the amount of Coconino Ss. present in the ejecta deposits is similar to the values of the total amount initially excavated. However, on the basis of the areal distribution of the units, it can be assumed that significant reworking and transport of the sandstone has occurred to a much larger extent than recent studies have stated. It appears that, on the basis of the extensive field and geophysical work done at the crater in the past, in conjunction with the results here, there has not been the 20–30 m erosion predicted by *Shoemaker* [1960]; however, there has been more reworking and erosion than the minimal amount stated by *Grant and Schultz* [1993].

4.6. Error Analysis

[41] The end-members fit the TIMS emissivity data to within 0.5% except for several areas throughout the scene. The RMS image reveals a region of high error located on the southern crater ejecta flap (Figure 6d). This area of Coconino Ss. ejecta is highly disturbed from the mining activities that once took place at the crater (Figure 2c). The error is due to a strong emissivity low in TIMS band 3, likely caused by fresh exposures of Coconino Ss. ejecta with no vegetation cover. Because these values fall outside the emissivity area defined by the original end-member spectra, this region is not linearly fit by the retrieval algorithm and therefore has a high RMS error. Other areas of poor fit occur over the visitor center/museum roof and within drainages along the western crater wall. The spectra of these drainages show a minor absorption in band 6 and therefore are not modeled linearly by the chosen end-members. Calcite does contain a small absorption band in this wavelength region that typically is not visible on the six-point TIMS spectra [*Crowley and Hook*, 1996]. Weathering of the Kaibab Fm. is an obvious source for calcite, but it remains unclear why this feature is not present throughout the rest of the image where the Kaibab Fm. occurs.

[42] Three random points were chosen around the ejecta blanket (Figure 1b), and the end-member percentages for each line were extracted and compared. Values from each location varied from 1 to 15% with altitude (Figure 9). The largest errors were associated with the Moenkopi Fm. fraction and may be related to the fact that these points were in locations with little Moenkopi Fm. ejecta. Therefore small changes in the end-member spectra produced proportionately larger variations in the model-predicted percentage. Similarly, the invariant nature of the Coconino Ss. end-member values reflects the dominance of its spectral features and its detection even at low spatial resolutions. The trends in the end-member percentages in Figure 9 indicate the potential effects associated with cross-contaminated spectra. Averaging the end-member values at each of the three sample locations and for each of the three spatial resolutions produced an overall error of 5.8%. This is approximately equal to the average decrease in the spectral resolution of the Coconino Ss. end-member ($\approx$6%). It appears that the degradation of the resolution, producing morphological changes in the end-member spectra, results in a linearly proportional error in deconvolution results.

5. Conclusions

[43] This initial application of this model to remotely gathered data using image-derived end-members is encouraging. The ability to detect subtle variations and patterns within the Meteor Crater ejecta deposits validates its potential for geologic mapping of complexly mixed terrain. The use of image end-members rather than laboratory or library spectra is advantageous in certain situations where a priori knowledge of the area is limited or rapid examination of the image is required. Further, by using rocks rather than minerals as end-members, image-derived maps will compare closely to those of existing geologic surveys and eliminate the need to maintain an unreasonably large spectral library. Lithologic units can also function as training sites for further, more detailed, mineral deconvolution using library derived spectral end-members.

[44] The results of this study indicate that the primary ejecta from the sedimentary units is still present in areas several crater radii (up to 1.2 km) from the rim. This finding supports the previous work by *Grant and Schultz* [1993], suggesting a lower amount of erosion has taken place than early investigations predicted. In addition, smaller discontinuous ejecta lobes, mentioned in recent studies as indicative of low erosion rates, are visible in the end-member images. However, in order to generate the areal extent of the current wind streak, there had to be a larger amount of erosion than predicted by *Grant and Schultz* [1993]. Their study as well as others at Meteor Crater concentrated only within several crater radii, whereas this approach has examined the far field ($\approx$3 km) as well. Concentrated primarily in the northeast trending wind streak, the Coconino Ss. is derived from eolian weathering and transport of the friable near-rim ejecta to the south of Meteor Crater. Arguments for higher amounts of initial ejecta and later erosion, on the other hand, can only be made if the erosion rates were appreciably greater in the past, thereby totally removing the Coconino Ss. ejecta entirely from the region. Although the climate has varied considerably with much wetter periods than at present [*Forester*, 1987], no evidence exists of major erosional episodes at the crater. Results of this study therefore indicate that the average erosion in the region may fall somewhere between previous estimates, with the near-rim ejecta subject to higher alteration and transport, and the distal units experiencing far less total vertical erosion.

[45] Resolution degradation from 3.2 to 10.9 m/pixel resulted in clear contamination of the end-member choices; however, the effects on the model results were negligible. Images still showed the same coherent mixing patterns, and the resultant end-member values for a given location varied by 6% on average. This implies that TIR data with lower spatial resolution such as ASTER and THEMIS would still yield valid and useful results where subjected to a linear retrieval analysis. However, the choice of the end-member location relies on the informed decision of the scientists performing the analysis.

[46] Analysis of weathering and erosion by remote-sensing techniques such as this one, together with detailed field studies, will greatly improve our understanding of crater deterioration on Earth. It may then be possible to apply those results to make predictions of surface weathering processes on Martian craters using the THEMIS instrument. The arguments of ejecta volume and thickness cannot all be addressed through linear retrieval of thermal infrared data. However, it can produce accurate surficial ejecta unit maps, and, on the basis of theoretical depth estimates, can be used as a proxy to derive an ejecta volume. Such techniques will be well suited for deciphering the large volumes of data soon to be returned from Mars from the THEMIS experiment [*Christensen et al.*, 1999] and from remote regions of Earth using ASTER instrument [*Kahle et al.*, 1991; *Yamaguchi et al.*, 1998]. Because both have a much lower spatial resolution than the TIMS data, these investigations must be made cautiously and not be overinterpreted.

[47] **Acknowledgments.** I would like to thank Philip Christensen and Kenneth Edgett for helpful discussions and early critiques of this work as well as sparking my initial interest in the Meteor Crater area. This work has also been greatly improved through discussions with John Grant, comments from Vincent Realmuto and one anonymous reviewer, and made possible by the dedication of the entire crew of the (now defunct) NASA C-130 aircraft program in acquiring the original TIMS data sets. Research funding for this study has been provided by NASA through the ASTER science project, the Planetary Geology and Geophysics program, and the Thermal Emission Spectrometer science project.

References

Abrams, M. J., E. Abbott, and A. B. Kahle, Combined use of visible, reflected infrared, and thermal infrared images for mapping Hawaiian lava flows, *J. Geophys. Res.*, *96*, 475–484, 1991.

Abrams, M., The Advanced Spaceborne Thermal Emission And Reflectance Radiometer (ASTER): Data products for the high spatial resolution imager on NASA's Terra platform, *Int. J. Remote Sens.*, *21*, 847–859, 2000.

Adams, J. B., M. O. Smith, and P. E. Johnson, Spectral mixture modeling: A new analysis of rock and soil types at the Viking Lander I site, *J. Geophys. Res.*, *91*, 8098–8112, 1986.

Bandfield, J. L., V. E. Hamilton, and P. R. Christensen, A Global view of Martian surface compositions from MGS-TES, *Science*, *287*, 1626–1630, 2000a.

Bandfield, J. L., P. R. Christensen, and M. D. Smith, Spectral data set factor analysis and end-member recovery: Application to analysis of Martian atmospheric particulates, *J. Geophys. Res.*, *105*, 9573–9587, 2000b.

Barbera, P. W., Geology of the Kelso-Baker Region, Mohave Desert, California using thermal infrared multi-spectral scanner data, M.S. thesis, 198 pp., Ariz. State Univ., Tempe, 1989.

Barringer, D. M., Coon Mountain and its crater, *Proc. Acad. Natl. Sci. Philos.*, *66*, 861–886, 1905.

Berke, A., L. S. Bernstein, and D. C. Robertson, MODTRAN: A moderate-resolution for LOWTRAN 7, *Rep. GL-TR-89-0122*, 38 pp., Geophys. Lab., Air Force Syst. Command, Hanscom Air Force Base, Hanscom, Mass., 1989.

Breed, C. S., J. F. McCauley, W. J. Breed, C. K. McCauley, and A. S. Cotera, Jr., Eolian (wind formed) landscapes, in *Landscapes of Arizona: The Geological Story*, edited by T. L. Smiley et al., 505 pp., University Press of America, New York, 1984.

Christensen, P. R., Martian dust mantling and surface composition: Interpretation of thermophysical properties, *J. Geophys. Res.*, *87*, 9985–9998, 1982.

Christensen, P. R., et al., Thermal Emission Spectrometer experiment: The Mars Observer Mission, *J. Geophys. Res.*, *97*, 7719–7734, 1992.

Christensen, P. R., B. M. Jakosky, H. H. Kieffer, M. C. Malin, H. Y. McSween, K. Nealson, G. Mehall, S. Silverman, and S. Ferry, The Thermal Emission Imaging System (THEMIS) instrument for the 2001 orbiter (abstract), *Lunar Planet. Sci.*, *XXX*, 1470, 1999.

Christensen, P. R., J. L. Bandfield, M. D. Smith, V. E. Hamilton, and R. N. Clark, Identification of a basaltic component on the Martian surface from Thermal Emission Spectrometer data, *J. Geophys. Res.*, *105*, 9609–9622, 2000a.

Christensen, P. R., et al., Detection of crystalline hematite mineralization on Mars by the Thermal Emission Spectrometer: Evidence of near-surface water, *J. Geophys. Res.*, *105*, 9623–9642, 2000b.

Christensen, P. R., J. L. Bandfield, V. E. Hamilton, D. A. Howard, M. D. Lane, J. L. Piatek, S. W. Ruff, and W. L. Stefanov, A thermal emission spectral library of rock-forming minerals, *J. Geophys. Res.*, *105*, 9735–9739, 2000c.

Croft, S. K., Cratering flow fields: Implications for the excavation and transient expansion stages of crater formation, *Proc. Lunar Planet. Sci. Conf.*, *11*, 2347–2378, 1980.

Crowley, J. K., and S. J. Hook, Mapping playa evaporite minerals and associated sediments in Death Valley, California, with multi-spectral thermal infrared images, *J. Geophys. Res.*, *101*, 643–660, 1996.

Crown, D. A., and C. M. Pieters, Spectral properties of plagioclase and pyroxene mixtures and the interpretation of lunar soil spectra, *Icarus*, *72*, 492–506, 1987.

Eastes, J. W., Spectral properties of halite-rich mineral mixtures: Implications for middle infrared remote sensing of highly saline environments, *Remote Sens. Environ.*, *27*, 289–304, 1989.

Edgett, K. S., and D. L. Anderson, For geologic investigations with airborne thermal infrared multi-spectral images: Transfer of calibration from laboratory spectrometer to TIMS as alternative for removing atmospheric effects, in *Summary of the Fifth Annual Airborne Earth Science Workshop*, vol. 2, edited by V. J. Realmuto, *JPL Publ. 957-*, 9–12, 1995.

Feely, K. C., and P. R. Christensen, Quantitative compositional analysis using thermal emission spectroscopy: Application to igneous and metamorphic rocks, *J. Geophys. Res.*, *104*, 24,195–24,210, 1999.

Forester, R. M., Late Quaternary paleoclimate records from lacustrine ostracodes, in *The Geology of North America*, vol. K-3, *North America and Adjacent Oceans During the Last Deglaciation*, edited by W. F. Ruddiman and H. E. Wright Jr., pp. 261–276, Geol. Soc. of Am., Boulder, Colo., 1987.

Garvin, J. B., J. L. Bufton, B. A. Campell, and S. H. Zisk, Terrain analysis of Meteor Crater ejecta blanket (abstract), *Lunar Planet. Sci.*, *XX*, 333–334, 1989.

Gillespie, A. R., A. B. Kahle, and F. D. Palluconi, Mapping alluvial fans in Death Valley, California, using multichannel thermal infrared images, *Geophys. Res. Lett.*, *11*, 1153–1156, 1984.

Gillespie, A. R., M. O. Smith, J. B. Adams, and S. C. Willis, Spectral mixture analysis of multi-spectral thermal infrared images, in *Proceedings of the Second Annual Airborne Earth Science Workshop*, vol. 2, edited by E. A. Abbott, *JPL Publ., 90-55*, 57–74, 1990a.

Gillespie, A. R., M. O. Smith, J. B. Adams, and S. C. Willis, A. F. Fischer III, and D. E. Sabol, Interpretation of residual images: Spectral mixture analysis of AVIRIS images, Owens Valley, California, in *Proceedings of the Second Annual Airborne Earth Science Workshop*, vol. 1, edited by R. A. Green, *JPL Publ., 90-54*, 1–28, 1990b.

Grant, J. A., and P. H. Schultz, The erosional state and style of Meteor Crater, Arizona (abstract), *Lunar Planet. Sci.*, *XX*, 355–356, 1989.

Grant, J. A., and P. H. Schultz, Characteristics of ejecta and alluvial deposits at Meteor Crater, Arizona and Odessa Craters, Texas: Results from ground penetrating radar (abstract), *Lunar Planet. Sci.*, *XXII*, 481–482, 1991.

Grant, J. A., and P. H. Schultz, Erosion of ejecta at Meteor Crater, Arizona, *J. Geophys. Res.*, *98*, 15,033–15,047, 1993.

Grieve, R. A. F., and J. B. Garvin, A geometric model for excavation and modification at terrestrial simple impact craters, *J. Geophys. Res.*, *89*, 11,561–11,572, 1984.

Hamilton, V. E., and P. R. Christensen, Determining the modal mineralogy of mafic and ultramafic igneous rocks using thermal emission spectroscopy, *J. Geophys. Res.*, *105*, 9717–9733, 2000.

Hook, S. J., A. R. Gabell, A. A. Green, and P. S. Kealy, A comparison of techniques for extracting emissivity information from thermal infrared data for geologic studies, *Remote Sens. Environ.*, *42*, 123–135, 1992.

Hook, S. J., K. E. Karlstrom, C. F. Miller, and K. J. W. McCaffrey, Mapping the Piute Mountains, California, with thermal infrared multi-spectral scanner (TIMS) Images, *J. Geophys. Res.*, *99*, 15,605–15,622, 1994.

Hook, S. J., J. J. Myers, K. F. Thome, M. Fitzgerald, and A. B. Kahle, The MODIS/ASTER airborne simulator (MASTER): A new instrument for earth science studies, *Remote Sens. Environ.*, *76*, 93–102, 2001.

Hunt, G. R., Electromagnetic radiation: The communication link in remote sensing, in *Remote Sensing in Geology*, edited by B. S. Siegel and A. R. Gillespie, pp. 5–45, John Wiley, New York, 1980.

Johnson, P. E., M. O. Smith, S. Taylor-George, and J. B. Adams, A semi-empirical method for analysis of the reflectance spectra of binary mineral mixtures, *J. Geophys. Res.*, *88*, 3557–3561, 1983.

Kahle, A. B., Surface emittance, temperature, and thermal inertia derived from thermal infrared multi-spectral scanner (TIMS) data for Death Valley, California, *Geophysics*, *52*, 858–874, 1987.

Kahle, A. B., and A. F. H. Goetz, Mineralogic information from a new airborne thermal infrared multi-spectral scanner, *Science*, *222*, 24–27, 1983.

Kahle, A. B., F. D. Palluconi, S. J. Hook, V. J. Realmuto, and G. Bothwell, The advanced spaceborne thermal emission and reflectance radiometer (ASTER), *Int. J. Imaging Sys. Tech.*, *3*, 144–156, 1991.

Kieffer, H. H., S. C. Chase, E. D. Miner, F. D. Palluconi, G. Muench, G. Neugebauer, and T. Z. Martin, Infrared thermal mapping of the Martian surface and atmosphere: First results, *Science*, *193*, 780–786, 1976.

Kieffer, H. H., T. Z. Martin, A. R. Peterfreund, B. M. Jakosky, E. D. Miner, and F. D. Palluconi, Thermal and albedo mapping of Mars during the Viking primary mission, *J. Geophys. Res.*, *82*, 4249–4291, 1977.

Lyon, R. J. P., Analysis of rocks by spectral infrared emission (8 to 25 microns), *Econ. Geol.*, *60*, 715–736, 1965.

McKee, E. D., The Coconino sandstone: Its history and origin, *Carnegie Inst. Washington, Publ.*, *440*, 77–115, 1934.

McKee, E. D., The environment and history of the Toroweap and Kaibab Formations of northern Arizona and southern Utah, *Carnegie Inst. Washington Publ.*, *492*, 268 pp., 1938.

McKee, E. D., Stratigraphy and history of the Moenkopi Formation of Triassic age, *Geol. Soc. Am. Mem.*, *61*, 133 pp., 1954.

Nishiizumi, K., C. P. Kohl, E. M. Shoemaker, J. R. Arnold, J. Klein, D. Fink, and R. Middleton, In situ ^{10}Be-^{26}Al exposure ages at Meteor Crater, Arizona, *Geochim. Cosmochim. Acta*, *55*, 2699–2703, 1991.

Palluconi, F. D., and G. R. Meeks, Thermal infrared multi-spectral scanner (TIMS): An investigators guide to TIMS data, *JPL Publ.*, *85–32*, 14 pp., 1985.

Pilon, J. A., R. A. F. Grieve, and V. L. Sharpton, The subsurface character of Meteor Crater, Arizona, as determined by ground-probing radar, *J. Geophys. Res.*, *96*, 15,563–15,576, 1991.

Presley, M. A., and P. R. Christensen, The effect of bimodal and polymodal mixtures of particle sizes on the thermal conductivity of particulate materials under Martian atmospheric pressures, (abstract), *Lunar Planet. Sci.*, *XXVII*, 1055–1056, 1996.

Ramsey, M. S., Quantitative analysis of geological surfaces: A deconvolution algorithm for midinfrared remote sensing data, 276 pp., Ph.D. dissertation, Ariz. State Univ., Tempe, 1996.

Ramsey, M. S., and P. R. Christensen, The linear 'un-mixing' of laboratory infrared spectra: Implications for the thermal emission spectrometer (TES) experiment, Mars Observer, (abstract), *Lunar Planet. Sci.*, *XXIII*, 1127–1128, 1992.

Ramsey, M. S., and P. R. Christensen, Mineral abundance determination: Quantitative deconvolution of thermal emission spectra, *J. Geophys. Res.*, *103*, 577–596, 1998.

Ramsey, M. S., and J. H. Fink, Remote monitoring of volcanic domes: Detection of chemical, textural and thermal heterogeneities (abstract), *Eos Trans. AGU*, *75*, 716, 1994.

Ramsey, M. S., P. R. Christensen, N. Lancaster, and D. A. Howard, Identification of sand sources and transport pathways at the Kelso Dunes, California using thermal infrared remote sensing, *Geol. Soc. Am. Bull.*, *111*, 646–662, 1999.

Realmuto, V. J., Separating the effects of temperature and emissivity: Emissivity spectrum normalization, in *Proceedings of the Second Annual Airborne Earth Science Workshop*, vol. 2, edited by E. A. Abbott, *JPL Publ. 90-55*, 31–35, 1990.

Regan, R. D., and W. J. Hinze, Gravity and magnetic investigations of Meteor Crater, Arizona, *J. Geophys. Res.*, *80*, 776–788, 1975.

Roddy, D. J., Pre-impact geologic conditions, physical properties, energy calculations, meteorite and initial crater dimensions and orientations of joints, faults and walls at Meteor Crater, Arizona, *Proc. Lunar Planet. Sci. Conf., 9th*, 3891–3980, 1978.

Sabins, F. F., *Remote Sensing Principles and Interpretation*, 2nd ed., 449 pp., W. H. Freeman, New York, 1987.

Sabol, D. E., J. B. Adams, and M. O. Smith, Quantitative subpixel spectral detection of targets in multi-spectral images, *J. Geophys. Res.*, *97*, 2659–2672, 1992.

Salisbury, J. W., and D. M. D'Aria, Emissivity of terrestrial materials in the 8–14 μm atmospheric window, *Remote Sens. Environ.*, *42*, 83–106, 1992.

Salisbury, J. W., and L. S. Walter, Thermal infrared (2.5–13.5 μm) spectroscopic remote sensing of igneous rock types on particulate planetary surfaces, *J. Geophys. Res.*, *94*, 9192–9202, 1989.

Schultz, P. H., and J. A. Grant, Styles of ejecta emplacement, Meteor Crater (abstract), *Lunar Planet. Sci.*, *XX*, 972–973, 1989.

Shoemaker, E. M., Impact mechanics at Meteor Crater, Arizona, Ph.D. dissertation, 55 pp., Princeton Univ., Princeton, N. J., 1960.

Shoemaker, E. M., and S. W. Kieffer, Guidebook to the geology of Meteor Crater, Arizona, *Publ. 17*, 66 pp., Cent. for Meteorite Stud., Ariz. State Univ., Tempe, Ariz., 1974.

Thomson, J. L., and J. W. Salisbury, The mid-infrared reflectance of mineral mixtures (7–14 μm), *Remote Sens. Environ.*, *45*, 1–13, 1993.

Yamaguchi, Y., A. B. Kahle, H. Tsu, T. Kawakami, and M. Pniel, Overview of the Advanced Spaceborne Thermal Emission And Reflectance Radiometer (ASTER), *IEEE Trans. Geosci. Remote Sens.*, *36*, 1062–1071, 1998.

M. S. Ramsey, Department of Geology and Planetary Science, University of Pittsburgh, 200 SRCC Building, Pittsburgh, PA 15260, USA. (ramsey@ivis.eps.pitt.edu)